In-situ MOCVD Growth and Band Offsets of Al_2O_3 Dielectric on β-Ga_2O_3 and β-$(Al_xGa_{1-x})_2O_3$ thin films

A F M Anhar Uddin Bhuiyan[1,a)], Lingyu Meng[1], Hsien-Lien Huang[2], Jinwoo Hwang[2], and
Hongping Zhao[1,2,b)]

[1]*Department of Electrical and Computer Engineering, The Ohio State University, Columbus, OH 43210, USA*
[2]*Department of Materials Science and Engineering, The Ohio State University, Columbus, OH 43210, USA*
[a)]Email: bhuiyan.13@osu.edu [b)]Corresponding author Email: zhao.2592@osu.edu

Abstract

The in-situ metalorganic chemical vapor deposition (MOCVD) growth of Al_2O_3 dielectrics on β-Ga_2O_3 and β-$(Al_xGa_{1-x})_2O_3$ films is investigated as a function of crystal orientations and Al compositions of β-$(Al_xGa_{1-x})_2O_3$ films. The interface and film qualities of Al_2O_3 dielectrics are evaluated by high resolution X-ray diffraction (HR-XRD) and scanning transmission electron microscopy (HR-STEM) imaging, which indicate the growth of high quality amorphous Al_2O_3 dielectrics with abrupt interfaces on (010), (100) and ($\bar{2}01$) oriented β-$(Al_xGa_{1-x})_2O_3$ films. The surface stoichiometries of Al_2O_3 deposited on all orientations of β-$(Al_xGa_{1-x})_2O_3$ are found to be well maintained with a bandgap energy of 6.91 eV as evaluated by high resolution x-ray photoelectron spectroscopy, which is consistent with the atomic layer deposited (ALD) Al_2O_3 dielectrics. The evolution of band offsets at both in-situ MOCVD and ex-situ ALD deposited Al_2O_3/β-$(Al_xGa_{1-x})_2O_3$ are determined as a function of Al composition, indicating the influence of the deposition method, orientation, and Al composition of β-$(Al_xGa_{1-x})_2O_3$ films on resulting band alignments. Type II band alignments are determined at the MOCVD grown Al_2O_3/β-$(Al_xGa_{1-x})_2O_3$ interfaces for (010) and (100) orientations, whereas type I band alignments with relatively lower conduction band offsets are observed along ($\bar{2}01$) orientation. Results from this study on MOCVD growth and band offsets of amorphous Al_2O_3 deposited on differently oriented β-Ga_2O_3 and β-$(Al_xGa_{1-x})_2O_3$ films will potentially contribute to design and fabricate future high performance β-

Ga_2O_3 and β-$(Al_xGa_{1-x})_2O_3$ based transistors using MOCVD in-situ deposited Al_2O_3 as gate dielectric.

Keywords: Ultra-wide bandgap semiconductor, Al_2O_3 dielectric, β-$(Al_xGa_{1-x})_2O_3$ thin film, metalorganic chemical vapor deposition, band offsets

I. Introduction

Beta gallium oxide (β-Ga_2O_3) with its ultrawide bandgap (UWBG) energy (4.5-4.9 eV) and high internal critical breakdown field strength ($E_{br,\ predicted}$ = 8 MV/cm) has stimulated substantial research interests as an emerging semiconductor material for next generation high power electronics [1]. The controllable n-type doping of β-Ga_2O_3 with excellent transport properties and its availability of differently oriented ((010), (100), ($\bar{2}$01) and (001)) single crystal native substrates have paved the way for developing high performance lateral and vertical transistors, Schottky barrier diodes and ultraviolet photodetectors fabricated on high quality β-Ga_2O_3 epi-films [2-19]. Furthermore, alloying β-Ga_2O_3 with Al_2O_3 provides additional band gap engineering over a range of 4.87-8.82 eV [20], and thus a pathway towards enhanced mobility with better device performance based on β-Ga_2O_3/β-$(Al_xGa_{1-x})_2O_3$ heterostructures [21]. In addition to the successful demonstration of β-Ga_2O_3/β-$(Al_xGa_{1-x})_2O_3$ based modulation doped field effect transistors (MODFETs) [22-25], the higher predicted breakdown field strength (16 MV/cm for 80% Al content) [26] with controllable n-type doping of β-$(Al_xGa_{1-x})_2O_3$ [27-29] show a great potential for the development of high-power and high-frequency electronic devices surpassing the state-of-the-art.

In recent years, epitaxial development of β-$(Al_xGa_{1-x})_2O_3$ thin films [30-39] and the implementation of β-$(Al_xGa_{1-x})_2O_3$/β-Ga_2O_3 based MODFET devices [22-25] have made significant progresses. Metalorganic chemical vapor deposition (MOCVD) of β-$(Al_xGa_{1-x})_2O_3$ thin films on differently oriented β-Ga_2O_3 substrates such as (010) ($x \leq 0.35$) [28,30,34,35,38], (100) ($x \leq 0.52$) [31,32] and ($\bar{2}01$) ($x \leq 0.48$) [33,38] have been demonstrated. Molecular beam epitaxy (MBE) grown Si delta-doped MODFETs have been demonstrated with decent electron mobility (< 180 $cm^2/V.s$) and relatively high sheet charge density (5 x 10^{12} cm^{-2}) by using 18-20% Al composition in the β-$(Al_xGa_{1-x})_2O_3$ layer [22-24]. Recently, a room temperature Hall mobility of 111 $cm^2/V.s$ with sheet charge density of 1.06 x 10^{13} cm^{-2} was measured in MOCVD grown β-Ga_2O_3/β-$(Al_{0.27}Ga_{0.73})_2O_3$ modulation-doped heterostructures [25]. To achieve higher density two-dimensional electron gases (2DEGs), high Al incorporation in β-$(Al_xGa_{1-x})_2O_3$ layer with larger β-Ga_2O_3/β-$(Al_xGa_{1-x})_2O_3$ band offset is required. Apart from the different incorporation efficiency of Al composition in differently oriented β-$(Al_xGa_{1-x})_2O_3$ thin films [28,31,33], the experimentally measured band offsets at β-Ga_2O_3/β-$(Al_xGa_{1-x})_2O_3$ heterointerfaces also exhibited a strong dependence on the substrate orientation [38]. The (100) orientated β-Ga_2O_3/β-$(Al_xGa_{1-x})_2O_3$ heterointerfaces showed relatively higher conduction band offsets as compared to (010) and ($\bar{2}01$) orientations [32,38], indicating potential opportunities for excellent carrier confinement along (100) orientation.

While high quality and high-Al content β-$(Al_xGa_{1-x})_2O_3$ films with larger β-Ga_2O_3/β-$(Al_xGa_{1-x})_2O_3$ band offsets are advantageous for carrier confinement at the heterointerfaces, the quality of the dielectric-semiconductor interface is crucial for reliable high-performance transistors. Several gate dielectric materials such as Al_2O_3, HfO_2, SiO_2 and their alloys or bilayer combinations have been extensively investigated in β-Ga_2O_3 based metal oxide-semiconductor field effect transistors (MOSFETs) [40-45]. While high quality dielectric material with high dielectric constant and lower concentration of interface and bulk traps can significantly improve the performance of β-Ga_2O_3

and β-$(Al_xGa_{1-x})_2O_3$ based devices, the higher conduction band offset (> 1 eV) at dielectric/β-Ga_2O_3 (or β-$(Al_xGa_{1-x})_2O_3$) interfaces is also expected for developing MOS structures with large breakdown field and lower gate leakage. Due to its good compatibility with β-Ga_2O_3, Al_2O_3 with a dielectric constant of 7 - 8.5 has been widely used as a gate dielectric in β-Ga_2O_3 and β-$(Al_xGa_{1-x})_2O_3$ based devices. Excellent transistor performance in terms of high figure of merits with large breakdown field strength has been demonstrated in (010) and (001) oriented β-Ga_2O_3 based lateral and vertical FET structures using atomic layer deposited (ALD) Al_2O_3 as gate dielectric [15,46,47,48]. However, such ex-situ deposition of Al_2O_3 dielectrics using ALD or sputtering might result in interface contamination due to the exposure of the surface of β-Ga_2O_3 or β-$(Al_xGa_{1-x})_2O_3$ epi-films to the ambient during loading the samples into different chamber to deposit gate dielectrics. Instead, the in-situ deposition of gate dielectric can potentially avoid such surface or interface contamination of the epi-layer by avoiding the exposure to the ambient atmosphere. Recently, MOCVD in-situ Al_2O_3 deposition on β-Ga_2O_3 is demonstrated with reduced interface traps as compared to the commonly used ALD technique [49], indicating a great potential for depositing high quality gate dielectrics using MOCVD. Moreover, the high temperature deposition of MOCVD (450-1000 °C) with higher deposition rates can improve the quality of the bulk dielectric materials with reduced trap density at the interface. From previous studies, MOCVD in situ growth of amorphous Al_2O_3 on GaN has been demonstrated with lower trap densities (7.4×10^{11} $cm^{-2}eV^{-1}$) and very small hysteresis as compared to the ex-situ ALD Al_2O_3 (1.6×10^{12} $cm^{-2}eV^{-1}$) on GaN MOSCAPs [50]. One of the motivations of this study is to explore the feasibility of in-situ MOCVD growth of amorphous Al_2O_3 on β-Ga_2O_3 and β-$(Al_xGa_{1-x})_2O_3$, since majority of the dielectric Al_2O_3 on Ga_2O_3 based transistors was deposited by ex-situ ALD. However, further studies are still required to investigate the influence of MOCVD growth conditions on the device performance while using the in-situ Al_2O_3 as the gate dielectric in transistors. Indeed, MOCVD can provide a wide range of growth conditions that can lead to different interface properties between Al_2O_3 and Ga_2O_3 or $(Al_xGa_{1-x})_2O_3$. The prior report on ALD deposited Al_2O_3 on (010) β-Ga_2O_3 films revealed the formation of crystalline interlayers of γ-phase Al_2O_3 with 1-5 nm thickness at the interface of Al_2O_3 and β-Ga_2O_3 with lower interface state densities than those of the amorphous Al_2O_3/(-201) β-Ga_2O_3 interface [51], indicating the potential of achieving high quality interfaces due to the crystallization of amorphous Al_2O_3. While MOCVD growth of Al_2O_3 dielectric is demonstrated on both β-Ga_2O_3 [49] and GaN [50, 52] semiconductors, the investigation of the interface quality of in-situ MOCVD deposited Al_2O_3/β-$(Al_xGa_{1-x})_2O_3$ interfaces are still lacking. Considering the highly orientation dependent band offsets at β-Ga_2O_3/β-$(Al_xGa_{1-x})_2O_3$ interfaces [38], the investigation of the material quality of Al_2O_3 dielectric deposited on differently oriented β-$(Al_xGa_{1-x})_2O_3$ interfaces with different Al compositions are still in need. Moreover, the accurate extraction of the band offsets at dielectric/β-$(Al_xGa_{1-x})_2O_3$ interface is also critical for designing and fabricating β-$(Al_xGa_{1-x})_2O_3$ based devices. Nevertheless, information related to the band discontinuities at the interface of Al_2O_3 dielectric and differently oriented β-$(Al_xGa_{1-x})_2O_3$ as a function of Al composition are not reported yet.

In this work, we have systematically investigated the interface quality of in-situ MOCVD grown Al_2O_3 dielectric on (010), (100) and $(\bar{2}01)$ oriented β-Ga_2O_3 and β-$(Al_xGa_{1-x})_2O_3$ thin films and experimentally determined the band offsets at Al_2O_3(dielectric)/β-$(Al_xGa_{1-x})_2O_3$ heterointerfaces with various Al compositions along different orientations. Moreover, the band offsets determined for MOCVD in-situ Al_2O_3 are also compared with ALD (ex-situ) Al_2O_3 deposited on β-$(Al_xGa_{1-x})_2O_3$ interfaces.

II. Experimental Section

The β-$(Al_xGa_{1-x})_2O_3$ thin films were grown on Fe doped semi-insulating (010), (100), and ($\bar{2}$01) oriented β-Ga_2O_3 substrates (purchased from Novel Crystal Technology, Inc), with an unintentionally doped (UID) ~ 65 nm thick β-Ga_2O_3 as buffer layer via Agnitron Technology Agilis R&D MOCVD system. Triethylgallium (TEGa), Trimethylaluminum (TMAl), and pure O_2 were used as Ga, Al, and O precursors, respectively. Argon (Ar) was used as the carrier gas. The different Al compositions (x = 0 - 52%) of differently oriented β-$(Al_xGa_{1-x})_2O_3$ films were obtained by systematically tuning the [TMAl]/[TMAl+TEGa] molar flow ratio, growth temperature (880 °C), chamber pressure (20-80 torr) and group VI/III ratio [28,30,31,33]. To minimize potential contaminations from the growth surface, all substrates were cleaned ex-situ by using solvents and then in-situ by high temperature (920°C) annealing for 5 mins under O_2 atmosphere before the growths start. On top of the β-$(Al_xGa_{1-x})_2O_3$ thin films, a 40 nm thick Al_2O_3 dielectric layer was deposited in the same MOCVD chamber at a growth temperature of 700 °C and chamber pressure of 20 torr. The O_2 flow rate was fixed at 500 sccm. The Al_2O_3 deposition rate of 4 nm/min was obtained with TMAl molar flow rate of 5.46 μmol/min. For the band offset measurements by using XPS, three types of samples were prepared as shown in Figure S1 of the supplementary material: (a) 20-60 nm thick β-$(Al_xGa_{1-x})_2O_3$ films grown on UID β-Ga_2O_3 buffer layer on top of (010), (100) and ($\bar{2}$01) β-Ga_2O_3 substrates, (b) ~ 40 nm thick, and (c) thin (~2-5 nm) Al_2O_3 deposited on (010), (100) and ($\bar{2}$01) oriented β-$(Al_xGa_{1-x})_2O_3$ films with different Al compositions. The ALD deposition of Al_2O_3 was performed in a Picosun SUNALE R-150B by using Trimethylaluminum (TMAl) as the Al precursor and water (H_2O) as the O_2 precursor. For the band offset measurements, on top of the MOCVD grown differently oriented β-$(Al_xGa_{1-x})_2O_3$ films, Al_2O_3 layers with thick (~50 nm) and thin (~3 nm) thicknesses were deposited at 300 °C in the ALD chamber. Prior to the loading into the ALD chamber, all β-$(Al_xGa_{1-x})_2O_3$ samples were cleaned using acetone, IPA, and DI water.

High resolution XRD using a Bruker D8 Discover was performed to evaluate the quality and structures of Al_2O_3 dielectrics and β-$(Al_xGa_{1-x})_2O_3$ epi-films oriented along different directions. Surface morphologies were evaluated by atomic force microscopy (AFM) using Bruker AXS Dimension Icon. Surface stoichiometry, band gap energies and band offsets at Al_2O_3/β-$(Al_xGa_{1-x})_2O_3$ were determined using XPS measurements with an energy resolution of 0.1 eV. A Kratos Axis Ultra X-ray photoelectron spectrometer using monochromic Al Kα x-ray source with a photon energy of 1486.6 eV was used for the XPS measurement. C 1s peak (284.8 eV) from the adventitious carbon was used as a reference to calibrate the binding energy. As the bandgaps and band offsets at Al_2O_3/β-$(Al_xGa_{1-x})_2O_3$ were determined using the binding energy differences between the core level peak positions of any given sample, the correction of the peak positions does not impact the results. The electron pass energy was set at 20 eV during high resolution scanning and 80 eV for survey scanning. A Thermo Fisher Scientific Themis-Z scanning transmission electron microscope (200 kV, Cs3=0.002 mm, and Cs5=1.0 mm) with probe convergence half angles of 17.9 mrad was utilized to perform high resolution STEM high angle annular dark filed (HAADF) imaging.

III. Results and Discussions

To evaluate the crystalline phase and quality of the in-situ MOCVD deposited Al_2O_3 dielectrics grown on differently oriented β-Ga_2O_3 thin films, high resolution XRD was performed. Figures 1 (a)-(c) show the XRD ω-2θ scans of the ~ 40 nm thick Al_2O_3 dielectrics deposited on top of 65 nm thick UID β-Ga_2O_3 buffer layer on (100), $(\bar{2}01)$ and (010) oriented β-Ga_2O_3 substrates, respectively. The Al_2O_3 dielectrics were deposited at a growth temperature of 700 °C. While high intensity distinguishable peaks originated from differently oriented β-Ga_2O_3 substrates are observed for all orientations, no other well-resolved XRD peaks corresponding to different crystalline phases/orientations of Al_2O_3 films are visible in wide range scans, indicating that the MOCVD deposited Al_2O_3 films possess amorphous structures for all different orientations of substrates, which is also evidenced from STEM imaging as discussed in the later sections. Our previous studies demonstrated the growth of γ-phase Al_2O_3 thin films on (010) β-Ga_2O_3 substrate at relatively higher growth temperature (880 °C) [30], suggesting that the lower growth temperature (700 °C) is a key parameter that can lead to the deposition of amorphous Al_2O_3 dielectrics on β-Ga_2O_3. The surface RMS roughness of a gate dielectric is also a critical parameter that has a significant impact on device performance. Figures 2 (a)-(c) show the surface RMS roughness of ~ 40 nm thick Al_2O_3 dielectric deposited in MOCVD chamber on (010), (100) and ($\bar{2}01$) β-Ga_2O_3 films, respectively. Smooth and uniform surface morphologies of Al_2O_3 with RMS roughness of 1.42 nm (010), 1.25 nm (100), and 1.17 nm ($\bar{2}01$) are observed on differently oriented β-Ga_2O_3 films. The lowest surface morphologies observed on ($\bar{2}01$) β-Ga_2O_3 films as compared to those of (010) and (100) β-Ga_2O_3, indicating a strong dependence of the surface morphologies of top Al_2O_3 dielectrics on the orientations of β-Ga_2O_3 substrates.

The quality of Al_2O_3 dielectrics and the interfacial abruptness of MOCVD deposited Al_2O_3/β-Ga_2O_3 (β-$(Al_xGa_{1-x})_2O_3$) for different orientations are investigated using high-resolution STEM imaging and energy dispersive x-ray spectroscopy (STEM-EDS) elemental mapping. High resolution HAADF STEM images for Al_2O_3/(010) β-Ga_2O_3 and Al_2O_3/(010) β-$(Al_{0.17}Ga_{0.83})_2O_3$ are shown in Figures 3 (a) and (b), respectively. The high resolution HAADF-STEM images of Al_2O_3 dielectric deposited on ($\bar{2}01$) and (100) oriented β-Ga_2O_3 and β-$(Al_{0.17}Ga_{0.83})_2O_3$ thin films are also shown in Figures 3 (c) and (d) [($\bar{2}01$) orientation] and (e) and (f) [(100) orientation], respectively. The growth of amorphous Al_2O_3 dielectrics on top of β-Ga_2O_3 and β-$(Al_{0.17}Ga_{0.83})_2O_3$ layers is confirmed from the atomic resolution STEM images. The sharp contrasts between Al_2O_3 dielectric (dark) and β-Ga_2O_3 (β-$(Al_{0.17}Ga_{0.83})_2O_3$) (bright) indicate high quality interfaces along all investigated orientations.

STEM-EDS spectroscopy also reveals abrupt and sharp interfaces between Al_2O_3 and (010) oriented β-Ga_2O_3 and β-$(Al_{0.17}Ga_{0.83})_2O_3$ as shown in Figures 4 (a-h) and Figures S2 and S3 of the supplementary materials. The EDS color maps of Ga (green) and Al (blue) elements in Figures 4 (a-d) [Al_2O_3/β-Ga_2O_3] and (e-h) [Al_2O_3/β-$(Al_{0.17}Ga_{0.83})_2O_3$] and elemental mapping (Figs. 4 (d) and (h)) also confirm the interfacial abruptness between Al_2O_3 and (010) oriented β-Ga_2O_3 (β-$(Al_{0.17}Ga_{0.83})_2O_3$). Figures 5 (a-d) and (e-h) show the HAADF-STEM images of Al_2O_3/($\bar{2}01$) β-Ga_2O_3 (Fig. 5(a)) and Al_2O_3/($\bar{2}01$) β-$(Al_{0.17}Ga_{0.83})_2O_3$ (Fig. 5(e)) interfaces with corresponding EDS maps of (b, f) Al, (c, g) Ga and (d, h) O elements. The abrupt transition of Ga and Al at Al_2O_3/($\bar{2}01$) β-Ga_2O_3 (β-$(Al_{0.17}Ga_{0.83})_2O_3$) interfaces are observed for both samples, as also shown in Figures S4 and S5 of the supplementary materials, with a very slight interdiffusion of Ga and Al atoms at the interfaces. The abruptness of the interfaces between Al_2O_3 and (100) oriented β-Ga_2O_3 (β-$(Al_xGa_{1-x})_2O_3$) is also evaluated by cross-sectional HAADF-STEM images and EDS elemental mapping of Al_2O_3/β-Ga_2O_3 and Al_2O_3/β-$(Al_{0.17}Ga_{0.83})_2O_3$ as shown in Figures 6 (a-d) and (e-h), (Figs. S6 and S7 of the supplementary materials) respectively. The EDS color maps of Al (blue) and Ga (green) components in Figures 6 (b, c) and (f, g) correspond to the Ga and Al concentrations of the samples as indicated by the EDS quantitative line scan (Figs. 6(d, h)) along the orange arrows in Figures 6 (a, e) reveal sharp and high-quality interfaces between Al_2O_3 dielectric and (100) oriented β-Ga_2O_3 (β-$(Al_{0.17}Ga_{0.83})_2O_3$) layers.

The surface stoichiometry of in-situ MOCVD deposited Al_2O_3 dielectric are investigated by using high resolution XPS. The O 1s, Al 2s and 2p core level data were used to determine the O and Al percentage in Al_2O_3 dielectric. Figures 7 (a-c) show the O 1s, Al 2s and Al 2p spectra for a representative Al_2O_3 film deposited on (010) β-Ga_2O_3. The peaks are fitted with Gaussian-Lorentzian function after subtracting by Shirley type background. The O 1s peak is fitted with two components, O-Al bond at 531.1 eV and O-H bond at 532.1 eV, as shown in Figure 7(a). The Al 2s and Al 2p core level peaks are fitted with single peak as shown in Figures 7(b) and (c), respectively. Using the relative sensitivity factors of O 1s, Al 2s and Al 2p peaks ($S_{O\ 1s} = 2.93$, $S_{Al\ 2s} = 0.753$ and $S_{Al\ 2p} = 0.5371$), the percentage of Al and O in Al_2O_3 dielectric is determined to be 40.39% and 59.61%, respectively. The list of all Al and O percentages in both MOCVD and ALD deposited Al_2O_3 on other orientations ((($\bar{2}01$)) and (100)) of β-Ga_2O_3 are included in Table S1 of the supplementary materials, indicating that the surface stoichiometries of Al_2O_3 deposited by using both MOCVD and ALD methods are well maintained on all investigated orientations.

By utilizing XPS, the bandgap of MOCVD deposited Al_2O_3 is estimated by measuring the onset of inelastic loss spectrum of O 1s core level peak. The estimation of the bandgap energies of wide bandgap semiconductor materials using the inelastic loss curve appeared on higher binding energy side of a high intensity XPS core level spectra is a well-established method [53-61]. The lower limit of inelastic scattering represents the bandgap of a material as the lowest energetically inelastic scattering that an electron experiences during its travelling from the bulk to the surface is the excitation from the valence band to the conduction band. Figure 8(a) shows the O 1s core level peak for a representative Al_2O_3 sample grown on (010) oriented β-Ga_2O_3 film. The onset is determined from the intersection of the linear extrapolation of the loss spectra curve and constant background as shown in Figure 8(b). The bandgap of MOCVD deposited Al_2O_3 is estimated as

6.91 eV from the separation between the onset and O 1s peak positions. Similarly, the ALD deposited Al_2O_3 also exhibited a bandgap energy of 6.88 eV, which is well consistent with the bandgap energy reported previously from different deposition methods [55-57, 62-64]. The bandgap determined by Reflection Electron Energy Loss Spectroscopy were estimated as 6.9 eV for Al_2O_3 deposited by either ALD or sputtering method [62-64], which are found to be very consistent with our extracted bandgap values by using XPS. Apart from these studies, the band gap of amorphous Al_2O_3 was determined to be 7.0 ± 0.1 eV by using Al 2p and O 1s photoelectron spectra [55]. In addition, 6.8 eV of bandgap energy were measured using O 1s core-level binding energy spectrum of ALD-Al_2O_3 on (010) Ga_2O_3 [56]. Similarly, from the energy separation between the main O 1s line and the loss threshold, a bandgap of 7.0 ± 0.1 eV was determined for the 120 nm thick Al_2O_3 film deposited on 6H-SiC [57]. These studies indicate that our measured bandgap of both MOCVD and ALD deposited Al_2O_3 are in a good agreement with previous reports. Using the same approach, the extraction of bandgap energies of (010), (100) and ($\bar{2}01$) oriented β-Ga_2O_3 and β-$(Al_xGa_{1-x})_2O_3$ with different Al compositions [38] are listed in Table S2 of the supplementary material.

The band offsets at the interfaces of Al_2O_3 with all three orientations ((010), (100) and ($\bar{2}01$)) of β-Ga_2O_3 and β-$(Al_xGa_{1-x})_2O_3$ for a wide Al composition range are determined by using XPS. The valence band offsets (ΔE_v) at Al_2O_3/β-Ga_2O_3 (β-$(Al_xGa_{1-x})_2O_3$) are determined by using the Kraut's method [65]. Using the bandgaps of Al_2O_3, β-Ga_2O_3 and β-$(Al_xGa_{1-x})_2O_3$ and ΔE_v values, the corresponding conduction band offsets (ΔE_c) are estimated as follows:

$$\Delta E_v = (E^{AlGaO}_{Ga\,3s} - E^{AlGaO}_{VBM}) - (E^{AlO}_{Al\,2p} - E^{AlO}_{VBM}) - (E^{AlGaO/AlO}_{Ga\,3s} - E^{AlGaO/AlO}_{Al\,2p}) \quad (1)$$

$$\Delta E_c = E^{AlO}_{g} - E^{AlGaO}_{g} - \Delta E_v \quad (2)$$

where $E_{\mathrm{Ga\ 3s}}^{\mathrm{AlGaO}}$ and $E_{Ga\ 3s}^{\mathrm{AlGaO/AlO}}$ are the binding energies of Ga 3s core levels in β-$(Al_xGa_{1-x})_2O_3$ bulk material and Al_2O_3/β-$(Al_xGa_{1-x})_2O_3$ interfaces, respectively. $E_{\mathrm{Al\ 2p}}^{\mathrm{AlO}}$ and $E_{\mathrm{Al\ 2p}}^{\mathrm{AlGaO/AlO}}$ are the Al 2p core level binding energies of Al_2O_3 bulk material and Al_2O_3/β-$(Al_xGa_{1.x})_2O_3$ interfaces, respectively. $E_{\mathrm{VBM}}^{\mathrm{AlGaO}}$ and $E_{\mathrm{VBM}}^{\mathrm{AlO}}$ are the valence band maxima (VBM) positions of β-$(Al_xGa_{1-x})_2O_3$ and Al_2O_3 bulk materials, respectively. $E_{\mathrm{g}}^{\mathrm{AlO}}$ and $E_{\mathrm{g}}^{\mathrm{AlGaO}}$ are the bandgap energies of the Al_2O_3 and β-$(Al_xGa_{1-x})_2O_3$ thin films, respectively.

The fitted Ga 3s, Al 2p core level peaks and the valence band (VB) spectra are shown in Figures 9(a)-(f) for the in-situ MOCVD deposited Al_2O_3 on (010) oriented β-$(Al_{0.17}Ga_{0.83})_2O_3$ thin films. The Ga 3s (Figs. 9(a) and (e)) and Al 2p (Figs. 9(c) and (f)) core level peak positions for bulk β-$(Al_{0.17}Ga_{0.83})_2O_3$ (Figs. 9(a)), Al_2O_3 (Figs. 9(c)) and Al_2O_3/β-$(Al_{0.17}Ga_{0.83})_2O_3$ heterostructure (Figs. 9(e) and (f)) are determined by fitting with mixed Lorentzian-Gaussian line shapes after applying the Shirley type background subtraction. Both Ga 3s and Al 2p core levels are fitted with the single peak. The VBM positions from bulk β-$(Al_{0.17}Ga_{0.83})_2O_3$ (Figs. 9(b)) and Al_2O_3 (Figs. 9(d)) are determined by the linear extrapolation of the leading edge of the VB spectra to the background. The ΔE_v of -0.18 eV is determined at the Al_2O_3/(010) β-$(Al_{0.17}Ga_{0.83})_2O_3$ interface by using equation (1). By using the ΔE_v value and bandgaps of Al_2O_3 and (010) β-$(Al_{0.17}Ga_{0.83})_2O_3$, the ΔE_c of 2.06 eV is determined from equation (2). Using similar approach, the band offsets at the interfaces between MOCVD (and ALD) deposited Al_2O_3 dielectrics and differently oriented β-Ga_2O_3 and β-$(Al_xGa_{1-x})_2O_3$ heterostructures for all investigated Al compositions are determined. The band offsets determined by using Ga 3s and Al 2p core levels are also verified by comparing with those extracted from Ga 3s /Ga 3d and Al 2p / Al 2s core levels as listed exemplarily for Al_2O_3/(010) β-$(Al_xGa_{1-x})_2O_3$ interfaces in Table 1 and Tables S2 and S3 of the supplementary material for other Al_2O_3/β-$(Al_xGa_{1-x})_2O_3$ interfaces along different orientations and deposition methods, indicating a good consistency between the band offsets values estimated from different core level spectra.

Heterostructures are classified as Type I and Type II depending on the alignment of the bands producing the discontinuity. While one material's band gap overlaps another's in Type I- straddling heterostructures, both conduction and valence band edges of a material are lower than the corresponding band edges of another material in Type II- staggered heterostructure. The band alignment diagram of MOCVD deposited Al_2O_3/β-Ga_2O_3 (β-$(Al_xGa_{1-x})_2O_3$) heterostructures are shown in Figures 10 (a)-(c) for (010), (100) and $(\bar{2}01)$ orientations, respectively. Type II (staggered) band alignment at the interfaces of Al_2O_3 deposited on (010) and (100) oriented β-$(Al_xGa_{1-x})_2O_3$ is determined for all investigated Al compositions, whereas the $(\bar{2}01)$ orientations show type I (straddling) band alignment between Al_2O_3 and β-$(Al_xGa_{1-x})_2O_3$. The valence band offsets are found to vary from -0.07 to -0.17 eV (010), -0.14 to -0.23 eV (100) and 0.20 to 0.27 eV $(\bar{2}01)$ with corresponding conduction band offsets ranging between 2.14 and 1.66 eV (010), 2.22 and 1.29 eV (100), and 1.79 to 0.9 eV $(\bar{2}01)$ as the Al compositions in differently oriented β-$(Al_xGa_{1-x})_2O_3$ are varied from 0 to 35% (010), 0 to 52% (100) and 0 to 48% $(\bar{2}01)$. Similarly, the evolution of the band alignments at the interfaces of ALD deposited Al_2O_3 with the MOCVD grown β-$(Al_xGa_{1-x})_2O_3$ with different Al compositions are shown in Figures 11 (a)-(c) for (010), (100) and $(\bar{2}01)$ orientations, respectively. As the Al composition varies, the valence and conduction band offsets range from -0.12 to -0.35 eV (ΔE_v) and 2.18 to 1.81 eV (ΔE_c) (for (010) orientation), -0.31 to -0.55 eV (ΔE_v) and 2.36 to 1.44 eV (ΔE_c) (for (100) orientation) and 0.07 to 0.29 eV (ΔE_v) and 1.74 to 0.89 eV (ΔE_c) (for $(\bar{2}01)$ orientation), respectively. Similar to the in-situ MOCVD deposited Al_2O_3, type II band alignments are observed for both (010) and (100) orientations and type I band discontinuity is observed at the interface of ALD $Al_2O_3/(\bar{2}01)$ β-$(Al_xGa_{1-x})_2O_3$. For both MOCVD and ALD deposition of Al_2O_3, the conduction band offsets exhibit relatively larger variations with Al compositions as compared to the valence band offsets for all three orientations. Such lower ΔE_v (0.25 eV) as compared to the conduction band offset (ΔE_c) of 2.06 eV was also demonstrated between the interface of amorphous Al_2O_3 and monoclinic β-Ga_2O_3 [66] by using the band-edge position information of amorphous Al_2O_3 from experimentally determined band gap and valence-band offset with corundum α-phase Al_2O_3 [55].

The evolution of the valence and conduction band offsets of both in-situ MOCVD and ALD grown Al_2O_3 dielectrics on β-$(Al_xGa_{1-x})_2O_3$ heterointerfaces are represented in Figures 12 (a)-(d) as a function of Al composition for different orientations. The general trend shows that both ΔE_v and ΔE_c values decrease as the Al compositions in β-$(Al_xGa_{1-x})_2O_3$ increases, with a much weaker variation in the ΔE_v values as compared to the corresponding changes in ΔE_c values. Although both deposition methods showed type II band discontinuity along (010) and (100) orientations and type I band alignment along $(\bar{2}01)$ orientations, the variations in the values of ΔE_v and ΔE_c between MOCVD and ALD deposited Al_2O_3/β-$(Al_xGa_{1-x})_2O_3$ heterointerfaces can be attributed to the quality of the bulk Al_2O_3 and Al_2O_3/β-$(Al_xGa_{1-x})_2O_3$ interfaces as the deposition of Al_2O_3 is performed under completely different growth environments. Previously, type I straddling gap band alignment was demonstrated on ALD Al_2O_3 on $(\bar{2}01)$ β-Ga_2O_3, whereas sputtered Al_2O_3 showed a type II staggered gap with β-Ga_2O_3 [62]. Similar changes of band alignment from type I to type II are also observed as the Al_2O_3 deposition methods changed from ALD to sputtering on (010) β-$(Al_{0.14}Ga_{0.86})_2O_3$ interfaces [64], revealing a strong influence of the synthesis method on the resulting band alignment. In this work, for both MOCVD and ALD deposition, the $Al_2O_3/(\bar{2}01)$ β-$(Al_xGa_{1-x})_2O_3$ interfaces show the smallest conduction band offsets as compared to the (010) and (100) orientations, with a type I band alignment (Figs. 12(b,d)). While a small variation in ΔE_v (Fig. 12(a)) and ΔE_c (Fig. 12(b)) values between the (010) and (100) orientations are observed for in-situ MOCVD deposited $Al_2O_3/\beta\text{-}(Al_xGa_{1-x})_2O_3$ interfaces, the ALD deposited Al_2O_3 on (100) oriented $\beta\text{-}(Al_xGa_{1-x})_2O_3$ exhibits relatively higher ΔE_v (Fig. 12(c)) and ΔE_c (Fig. 12(d)) values as compared to other orientations, indicating a strong dependence of the band offsets on dielectric deposition methods, crystalline orientations and Al compositions of $\beta\text{-}(Al_xGa_{1-x})_2O_3$ films.

IV. Conclusion

In summary, in-situ MOCVD growth of Al_2O_3 dielectrics with high quality $Al_2O_3/\beta\text{-}(Al_xGa_{1-x})_2O_3$ interfaces are successfully demonstrated on different orientations of $\beta\text{-}(Al_xGa_{1-x})_2O_3$ as a function of Al composition. The growth of high quality amorphous Al_2O_3 dielectrics with sharp interfaces and good surface stoichiometry are revealed by comprehensive characterization of high resolution XRD, STEM and XPS. As compared to (010) and (100) orientations, relatively lower RMS roughness is observed for Al_2O_3 dielectrics deposited on $(\bar{2}01)$ $\beta\text{-}Ga_2O_3$, indicating an influence of crystal orientation of underlying $\beta\text{-}Ga_2O_3$ on the surface morphologies of top Al_2O_3 dielectric. The band offsets between in-situ MOCVD and ALD deposited Al_2O_3 dielectric and $\beta\text{-}(Al_xGa_{1-x})_2O_3$ interfaces are investigated systematically for a wide range of Al compositions, revealed a strong influence of deposition methods, orientations, and Al composition of $\beta\text{-}(Al_xGa_{1-x})_2O_3$ films on the valence and conduction band offsets. A type-II band alignment at $Al_2O_3/\beta\text{-}(Al_xGa_{1-x})_2O_3$ interfaces for all investigated Al compositions are observed for (010) and (100) oriented $\beta\text{-}(Al_xGa_{1-x})_2O_3$ films, whereas type-I band alignment is observed for $(\bar{2}01)$ orientation with relatively lower ΔE_c values for both deposition methods. A weaker variation in ΔE_v values with different Al compositions of $\beta\text{-}(Al_xGa_{1-x})_2O_3$ are observed as compared to the variation in ΔE_c

values. The high quality MOCVD growth of Al_2O_3 on differently oriented β-Ga_2O_3 and β-$(Al_xGa_{1-x})_2O_3$ films with sharp interfaces and the information on orientation dependent band offsets will be useful for the understanding, modeling and fabrication of β-Ga_2O_3 and β-$(Al_xGa_{1-x})_2O_3$ based MOS devices.

See the supplementary material for the schematic of the samples grown for band offset measurements, summary of the O and Al percentage of Al_2O_3 dielectrics calculated by using O 1s and Al 2p/Al 2s core level XPS spectra, and the summary of the band offsets at MOCVD in-situ and ALD ex-situ deposited Al_2O_3/β-$(Al_xGa_{1-x})_2O_3$ interfaces.

Conflict of Interest Statement

On behalf of all authors, the corresponding author states that there is no conflict of interest.

Supplementary Material

See supplementary material for XPS data for determining the band offsets and STEM-EDS maps.

Acknowledgements

The authors acknowledge the Air Force Office of Scientific Research FA9550-18-1-0479 (AFOSR, Dr. Ali Sayir) for financial support. The authors also acknowledge the National Science Foundation (Grant No. 1810041, No. 2019753) and Semiconductor Research Corporation (SRC) under the Task ID GRC 3007.001 for partial support. Electron microscopy was performed at the Center for Electron Microscopy and Analysis (CEMAS) at The Ohio State University.

Data Availability

The data that support the findings of this study are available from the corresponding author upon reasonable request.

References

1. A. J. Green, J. Speck, G. Xing, P. Moens, F. Allerstam, K. Gumaelius, T. Neyer, A. Arias-Purdue, V. Mehrotra, A. Kuramata, K. Sasaki, S. Watanabe, K. Koshi, J. Blevins, O. Bierwagen, S. Krishnamoorthy, K. Leedy, A. R. Arehart, A. T. Neal, S. Mou, S. A. Ringel, A. Kumar, A. Sharma, K. Ghosh, U. Singisetti, W. Li, K. Chabak, K. Liddy, A. Islam, S. Rajan, S. Graham, S. Cho, Z. Cheng, and M. Higashiwaki, APL Materials 10, 029201 (2022).
2. A. Kuramata, K. Koshi, S. Watanabe, Y. Yamaoka, T. Masui, and S. Yamakoshi, Jpn. J. Appl. Phys., Part 1 55, 1202A2 (2016).
3. Z. Feng, A F M A. U. Bhuiyan, M. R. Karim, and H. Zhao, Appl. Phys. Lett. 114, 250601 (2019).
4. H. Okumura, M. Kita, K. Sasaki, A. Kuramata, M. Higashiwaki, and J. S. Speck, Appl. Phys. Express 7, 095501 (2014).
5. E. Ahmadi, O. S. Koksaldi, S. W. Kaun, Y. Oshima, D. B. Short, U. K. Mishra and J. S. Speck, Appl. Phys. Express 10, 041102 (2017).
6. Z. Feng, A F M A. U. Bhuiyan, Z. Xia, W. Moore, Z. Chen, J. F. McGlone, D. R. Daughton, A. R. Arehart, S. A. Ringel, S. Rajan, and H. Zhao, Phys. Status Solidi RPL. 14, 2000145 (2020).
7. H. Ghadi, J. F. McGlone, Z. Feng, A. F. M. A. U. Bhuiyan, H. Zhao, A. R. Arehart, S. A. Ringel, Appl. Phys. Lett. 117, 172106 (2020).
8. A. Bhattacharyya, P. Ranga, S. Roy, J. Ogle, L. Whittaker-Brooks, and S. Krishnamoorthy, Applied Physics Letters 117, 142102 (2020).
9. G. Seryogin, F. Alema, N. Valente, H. Fu, E. Steinbrunner, A. T. Neal, S. Mou, A. Fine, and A. Osinsky, Appl. Phys. Lett. 117, 262101 (2020).
10. H. Ghadi, J. F. McGlone, C. M Jackson, E. Farzana, Z. Feng, A. F. M. A. U. Bhuiyan, H. Zhao, A. R Arehart, S. A. Ringel, APL Materials 8, 021111 (2020).
11. Z. Xia, H. Xue, C. Joishi, J. McGlone, N. K. Kalarickal, S. H. Sohel, M. Brenner, A. Arehart, S. Ringel, S. Lodha, W. Lu, and S. Rajan, IEEE Electron Device Lett. 40, 1052 (2019).
12. E. Farzana, F. Alema, W. Y. Ho, A. Mauze, T. Itoh, A. Osinsky, J. S Speck, Appl. Phys. Lett. 118, 162109 (2021).
13. Z. Hu, K. Nomoto, W. Li, N. Tanen, K. Sasaki, A. Kuramata, T. Nakamura, D. Jena, and H. G. Xing, IEEE Electron Device Lett. 39, 869 (2018).
14. M. Higashiwaki, K. Sasaki, A. Kuramata, T. Masui, and S. Yamakoshi, Appl. Phys. Lett. 100, 013504 (2012).

15. J. Green, K. D. Chabak, E. R. Heller, R. C. Fitch, Jr., M. Baldini, A. Fiedler, K. Irmscher, G. Wagner, Z. Galazka, S. E. Tetlak, A. Crespo, K. Leedy, and G. H. Jessen, IEEE Electron Device Lett. 37, 902 (2016).
16. T. Oshima, T. Okuno, N. Arai, N. Suzuki, S. Ohira, and S. Fujita, Appl. Phys. Express 1, 011202 (2008).
17. Z. Feng, A F M A. U. Bhuiyan, N. K. Kalarickal, S. Rajan, and H. Zhao, Phys. Appl. Phys. Lett. 117, 222106 (2020).
18. N. K Kalarickal, A. Fiedler, S. Dhara, H.-L. Huang, A F M A. U. Bhuiyan, M. W. Rahman, T. Kim, Z. Xia, Z. J. Eddine, A. Dheenan, M. Brenner, H. Zhao, J. Hwang, S. Rajan, Appl. Phys. Lett. 119, 123503 (2021).
19. Y. Zheng, Z. Feng, A F M A. U. Bhuiyan, L. Meng, S. Dhole, Q. Jia, H. Zhao, J.-H. Seo, J. Mater. Chem. C. 9, 6180 (2021).
20. H. Peelaers, J. B. Varley, J. S. Speck, and C. G. Van de Walle, Appl. Phys. Lett. 112, 242101 (2018).
21. K. Ghosh and U. Singisetti, J. Mater. Res. 32, 4142 (2017).
22. S. Krishnamoorthy, Z. Xia, C. Joishi, Y. Zhang, J. McGlone, J. Johnson, M. Brenner, A. R. Arehart, J. Hwang, S. Lodha, and S. Rajan, Appl. Phys. Lett. 111, 023502 (2017).
23. Y. Zhang, A. Neal, Z. Xia, C. Joishi, J. M. Johnson, Y. Zheng, S. Bajaj, M. Brenner, D. Dorsey, K. Chabak, G. Jessen, J. Hwang, S. Mou, J. P. Heremans, and S. Rajan, Appl. Phys. Lett. 112, 173502 (2018).
24. N. K. Kalarickal, Z. Feng, A F M A. U. Bhuiyan, Z. Xia, J. F. McGlone, W. Moore, A. R. Arehart, S. A. Ringel, H. Zhao, and S. Rajan, IEEE Transaction on Electron Devices, 68, 29-35 (2021).
25. P. Ranga, A. Bhattacharyya, A. Chmielewski, S. Roy, R. Sun, M. A Scarpulla, N. Alem, and S. Krishnamoorthy, Appl. Phys. Express 14, 025501 (2021).
26. J. B. Varley, J. Mater. Res. 36, 4790 (2021).
27. J. B. Varley, A. Perron, V. Lordi, D. Wickramaratne, and J. L. Lyons, Appl. Phys. Lett. 116, 172104 (2020).
28. A F M A. U. Bhuiyan, Z. Feng, J. M. Johnson, Z. Chen, H.-L. Huang, J. Hwang, and H. Zhao, Appl. Phys. Lett. 115, 120602 (2019).
29. A F M A. U. Bhuiyan, Z. Feng, L. Meng, A. Fiedler, H.-L. Huang, A. T. Neal, E. Steinbrunner, S. Mou, J. Hwang, S. Rajan and H. Zhao, "Si doping in MOCVD grown (010) β-$(Al_xGa_{1-x})_2O_3$ thin films" J. Appl. Phys. 131, 145301 (2022).
30. A F M A. U. Bhuiyan, Z. Feng, J. M. Johnson, H.-L. Huang, J. Sarker, M. Zhu, M. R. Karim, B. Mazumder, J. Hwang, and H. Zhao, APL Mater. 8, 031104 (2020).
31. A F M A. U. Bhuiyan, Z. Feng, J. M. Johnson, H.-L. Huang, J. Hwang, and H. Zhao, Cryst. Growth Des. 20, 6722 (2020).
32. A F M A. U. Bhuiyan, Z. Feng, J. M. Johnson, H.-L. Huang, J. Hwang, and H. Zhao, Appl. Phys. Lett. 117, 252105 (2020).

33. A F M A. U. Bhuiyan, Z. Feng, J. M. Johnson, H.-L. Huang, J. Hwang, and H. Zhao, Appl. Phys. Lett. 117, 142107 (2020).
34. A F M A. U. Bhuiyan, Z. Feng, L. Meng, H. Zhao, J. Mater. Res. 36, 4804 (2021).
35. J. M. Johnson, H.-L. Huang, M. Wang, S. Mu, J. B. Varley, A. F. M. A. U. Bhuiyan, Z. Feng, N. K. Kalarickal, S. Rajan, H. Zhao, C. G. Van de Walle, and J. Hwang, APL Materials 9, 051103 (2021).
36. A F M A. U. Bhuiyan, Z. Feng, J. M. Johnson, H.-L. Huang, J. Sarker, M. Zhu, M. R. Karim, B. Mazumder, J. Hwang, and H. Zhao, APL Materials 8 (8), 089102 (2020).
37. J. Sarker, A. F. M. A. U. Bhuiyan, Z. Feng, H. Zhao and B. Mazumder, J. Phys. D: Appl. Phys. 54, 184001 (2021).
38. A F M A. U. Bhuiyan, Z. Feng, H.-L. Huang, L. Meng, J. Hwang, H. Zhao, J. Vac. Sci. Technol. A 39, 063207 (2021).
39. J. Sarker, S. Broderick, A. F. M. A. U. Bhuiyan, Z. Feng, H. Zhao, and B. Mazumder, Appl. Phys. Lett. 116, 152101 (2020).
40. L. Yuan, H. Zhang, R. Jia, L. Guo, Y. Zhang, and Y. Zhang, Appl. Surf. Sci. 433, 530 (2018).
41. Z. (A.) Jian, I. Sayed, W. Liu, S. Mohanty, and E. Ahmadi, Appl. Phys. Lett. 118, 172102 (2021).
42. S. Sharma, K. Zeng, S. Saha, and U. Singisetti, IEEE Electron Device Lett. 41, 836 (2020).
43. P. H. Carey, F. Ren, D. C. Hays, B. P. Gila, S. J. Pearton, S. Jang, and A. Kuramata, Jpn. J. Appl. Phys., Part 1 56, 071101 (2017).
44. W. Li, K. Nomoto, Z. Hu, T. Nakamura, D. Jena, and H. G. Xing, in IEEE International Electron Devices Meeting (IEEE, San Francisco, CA, USA, 2019), pp. 12.4.1–12.4.4.
45. H. Dong, W. Mu, Y. Hu, Q. He, B. Fu, H. Xue, Y. Qin, G. Jian, Y. Zhang, S. Long, Z. Jia, H. Lv, Q. Liu, X. Tao, and M. Liu, AIP Adv. 8, 065215 (2018).
46. K. D. Chabak, N. Moser, A. J. Green, D. E. Walker Jr., S. E. Tetlak, E. Heller, A. Crespo, R. Fitch, J. P. McCandless, K. Leedy, M. Baldini, G. Wagner, Z. Galazka, X. Li, and G. Jessen, Appl. Phys. Lett. 109, 213501 (2016).
47. W. Li, K. Nomoto, Z. Hu, D. Jena, H. G. Xing, IEEE Electron Device Letters, 41, 107 (2020).
48. Z. Jian, S. Mohanty and E. Ahmadi, Appl. Phys. Lett. 116, 242105 (2020)
49. S. Roy, A. E. Chmielewski, A. Bhattacharyya, P. Ranga, R. Sun, M. A. Scarpulla, N. Alem, and S. Krishnamoorthy. Adv. Electron. Mater. 7, 2100333 (2021).
50. X. Liu, R. Yeluri, J. Kim, S. Lal, A. Raman, C. Lund, S. Wienecke, J. Lu, M. Laurent, S. Keller, and U. K. Mishra, Appl. Phys. Lett. 103, 053509 (2013).
51. T. Kamimura, D. Krishnamurthy, A. Kuramata, S. Yamakoshi, and M. Higashiwaki, Jpn. J. Appl. Phys. 55, 1202B5 (2016).
52. X. Liu, J. Kim, R. Yeluri, S. Lal, H. Li, J. Lu, S. Keller, B. Mazumder, J. S. Speck, and U. K. Mishra, J. Appl. Phys. 114, 164507 (2013).

53. M. T. Nichols, W. Li, D. Pei, G. A. Antonelli, Q. Lin, S. Banna, Y. Nishi, and J. L. Shohet, J. Appl. Phys. 115, 094105 (2014).
54. A F M Anhar Uddin Bhuiyan, Z. Feng, H.-L. Huang, L. Meng, J. Hwang, H. Zhao, APL Mater. 9, 101109 (2021).
55. E. O. Filatova and A. S. Konashuk, J. Phys. Chem. C 119, 20755 (2015).
56. T. Kamimura, K. Sasaki, M. H. Wong, D. Krishnamurthy, A. Kuramata, T. Masui, S. Yamakoshi, and M. Higashiwaki, Appl. Phys. Lett. 104, 192104 (2014).
57. K. Y. Gao, Th. Seyller, L. Ley, F. Ciobanu, G. Pensl, A. Tadich, J. D. Riley, and R. G. C. Leckey, Appl. Phys. Lett. 83, 1830 (2003).
58. K. Konishi, T. Kamimura, M. H. Wong, K. Sasaki, A. Kuramata, S. Yamakoshi, M. Higashiwaki, Phys. Status Solidi B 253 (4), 623 (2016).
59. Z. Feng, Q. Feng, J. Zhang, C. Zhang, H. Zhou, X. Li, L. Huang, L. Xu, Y. Hub, S. Zhao, Y. Hao, J. Alloys Compd 745, 292 (2018).
60. Y. Jia, K. Zeng, J. S. Wallace, J. A Gardella, U. Singisetti, Appl. Phys. Lett. 106, 102107 (2015).
61. Z. Feng, Q. Feng, J. Zhang, X. Li, F. Li, L. Huang, H.-Y. Chen, H.-L. Lu, Y. Hao, Appl. Surf. Sci. 434, 440 (2018).
62. P. H. Carey IV, F. Ren, D. C. Hays, B.P. Gila, S.J. Pearton, S. Jang, A. Kuramata, Vacuum 142, 52 (2017).
63. C. Fares, F. Ren, E. Lambers, D. C. Hays, B. P. Gila and S. J. Pearton, J. Electron. Mater. 48, 1568 (2019).
64. C. Fares, F. Ren, D. C. Hays, B. P. Gila, and S. J. Pearton, ECS J Solid State Sci 8 (7), Q3001 (2019).
65. E. A. Kraut, R. W. Grant, J. R. Waldrop, and S. P. Kowalczyk, Phys. Rev. Lett. 44, 1620 (1980).
66. T. Wang, W. Li, C. Ni, and A. Janotti, Phys. Rev. Appl. 10, 011003 (2018).

Table Caption

Table 1. Summary of the valence and conduction band offsets at Al_2O_3/(010) β-$(Al_xGa_{1-x})_2O_3$ interfaces, determined by using the VBM, Ga 3s, Ga 3d and Al 2p core level peak positions.

Figure Captions

Figure 1. XRD ω-2θ scans of in-situ MOCVD grown ~ 40 nm thick Al_2O_3 dielectrics on (a) (010), (b) ($\bar{2}01$), and (c) (100) β-Ga_2O_3 substrates.

Figure 2. Surface AFM images (scan area: 5x5 μm^2) of MOCVD deposited Al_2O_3 dielectrics on (a) (010), (b) ($\bar{2}01$), and (c) (100) β-Ga_2O_3 substrates.

Figure 3. High resolution HAADF-STEM cross-sectional images of in-situ MOCVD deposited Al_2O_3 dielectrics grown on (a) (010) β-Ga_2O_3, (b) (010) β-$(Al_{0.17}Ga_{0.83})_2O_3$, (c) ($\bar{2}01$) β-$Ga_2O_3$, (d) ($\bar{2}01$) β-$(Al_{0.17}Ga_{0.83})_2O_3$, (e) (100) β-$Ga_2O_3$, and (f) (100) β-$(Al_{0.17}Ga_{0.83})_2O_3$ layers. The HAADF-STEM images for Al_2O_3/(010) β-Ga_2O_3 (β-$(Al_{0.17}Ga_{0.83})_2O_3$) are taken from [001] zone axis and Al_2O_3/($\bar{2}01$) and (100) oriented β-Ga_2O_3 (β-$(Al_{0.17}Ga_{0.83})_2O_3$) are taken from [010] zone axis.

Figure 4. STEM-EDS maps for MOCVD deposited Al_2O_3 dielectrics on (a-d) (010) β-Ga_2O_3 and (e-h) (010) β-$(Al_{0.17}Ga_{0.83})_2O_3$. HAADF images of (a) Al_2O_3/(010) β-Ga_2O_3 and Al_2O_3/(010) β-$(Al_{0.17}Ga_{0.83})_2O_3$ with corresponding (b,f) Al and (c,g) Ga EDS maps and (d,h) atomic fraction elemental profiles as indicated by the orange arrow in (a, e).

Figure 5. STEM-EDS for maps MOCVD Al_2O_3 dielectrics deposited on (a-d) ($\bar{2}01$) β-Ga_2O_3 and (e-h) ($\bar{2}01$) β-$(Al_{0.17}Ga_{0.83})_2O_3$. HAADF images of (a) Al_2O_3/($\bar{2}01$) β-Ga_2O_3 and Al_2O_3/($\bar{2}01$) β-$(Al_{0.17}Ga_{0.83})_2O_3$ with corresponding (b,f) Al and (c,g) Ga EDS maps and (d,h) atomic fraction elemental profiles as indicated by the orange arrow in (a, e).

Figure 6. STEM-EDS maps for MOCVD Al_2O_3 dielectrics deposited on (a-d) (100) β-Ga_2O_3 and (e-h) (100) β-$(Al_{0.17}Ga_{0.83})_2O_3$. HAADF images of (a) Al_2O_3/(100) β-Ga_2O_3 and Al_2O_3/(100) β-

$(Al_{0.17}Ga_{0.83})_2O_3$ with corresponding (b,f) Al and (c,g) Ga EDS maps and (d,h) atomic fraction elemental profiles as indicated by the orange arrow in (a, e).

Figure 7. XPS (a) O 1s, (b) Al 2s and (c) Al 2p core level spectra for in-situ MOCVD grown Al_2O_3 dielectrics on (010) β-Ga_2O_3 substrates. Experimental data points (black open circles) are fitted using mixed Lorentzian-Gaussian line shapes (black solid lines) after applying the Shirley background (gray solid lines) subtraction.

Figure 8. (a) The bandgap energy estimated by using the onset of inelastic loss spectra of O 1s core level peak from in-situ MOCVD grown Al_2O_3 dielectrics on (010) β-$(Al_{0.17}Ga_{0.83})_2O_3$. (b) zoomed view of the background region of the O 1s core level.

Figure 9. Fitted (a) Ga 3s and (b) valence band (VB) spectra from (010) β-$(Al_{0.17}Ga_{0.83})_2O_3$ and (c) Al 2p and (d) VB spectra from ~40 nm thick Al_2O_3 deposited in-situ by MOCVD. The fitted Ga 3s and Al 2p core levels from Al_2O_3/(010) β-$(Al_{0.17}Ga_{0.83})_2O_3$ heterointerfaces are shown in (e) and (f), respectively. Experimental data are shown as black open circles and the fitted curves (envelope) are represented as black sloid lines.

Figure 10. The band alignments at the interfaces of in-situ MOCVD deposited Al_2O_3 and (a) (010) β-$(Al_xGa_{1-x})_2O_3$ ($x = 0 - 0.35$) (b) (100) β-$(Al_xGa_{1-x})_2O_3$ ($x = 0 - 0.52$) and (c) ($\bar{2}01$) oriented β-$(Al_xGa_{1-x})_2O_3$ ($x = 0 - 0.48$).

Figure 11. The band alignments at the interfaces of ALD deposited Al_2O_3 and (a) (010) β-$(Al_xGa_{1-x})_2O_3$ ($x = 0 - 0.35$) (b) (100) β-$(Al_xGa_{1-x})_2O_3$ ($x = 0 - 0.52$) and (c) ($\bar{2}01$) oriented β-$(Al_xGa_{1-x})_2O_3$ ($x = 0 - 0.48$).

Figure 12. The evolution of the (a,c) valence band offsets (considering the valence band maxima position of Al_2O_3 at 0 eV) and (b,d) conduction band offsets at the interfaces of (a,b) in-situ

MOCVD and (c,d) ALD deposited Al_2O_3 and differently oriented β-$(Al_xGa_{1-x})_2O_3$ as a function of Al compositions.

Table 1.

Ga 3s and Al 2p:

Sample	E_g (± 0.20 eV)	$E_{Ga\ 3s}^{AlGaO} - E_{VBM}^{AlGaO}$ (± 0.04 eV)	$E_{Al\ 2p}^{AlO} - E_{VBM}^{AlO}$ (± 0.04 eV)	$E_{Ga\ 3s}^{AlGaO/AlO} - E_{Al\ 2p}^{AlGaO/AlO}$ (± 0.02 eV)	ΔE_v (eV) (± 0.06 eV)	ΔE_c (eV) (± 0.29 eV)
Al_2O_3	6.91		71.23			
β-Ga_2O_3	4.84	157.43		86.27	-0.07	2.14
β-$(Al_{0.17}Ga_{0.83})_2O_3$	5.03	157.38		86.32	-0.18	2.06
β-$(Al_{0.35}Ga_{0.65})_2O_3$	5.42	157.47		86.40	-0.17	1.66

Ga 3d and Al 2p:

Sample	E_g (± 0.20 eV)	$E_{Ga\ 3d}^{AlGaO} - E_{VBM}^{AlGaO}$ (± 0.04 eV)	$E_{Al\ 2p}^{AlO} - E_{VBM}^{AlO}$ (± 0.04 eV)	$E_{Ga\ 3d}^{AlGaO/AlO} - E_{Al\ 2p}^{AlGaO/AlO}$ (± 0.02 eV)	ΔE_v (eV) (± 0.06 eV)	ΔE_c (eV) (± 0.29 eV)
Al_2O_3	6.91		71.23			
β-Ga_2O_3	4.84	16.87		-54.32	-0.05	2.12
β-$(Al_{0.17}Ga_{0.83})_2O_3$	5.03	16.79		-54.30	-0.14	2.02
β-$(Al_{0.35}Ga_{0.65})_2O_3$	5.42	16.87		-54.24	-0.12	1.61

Figure 1.

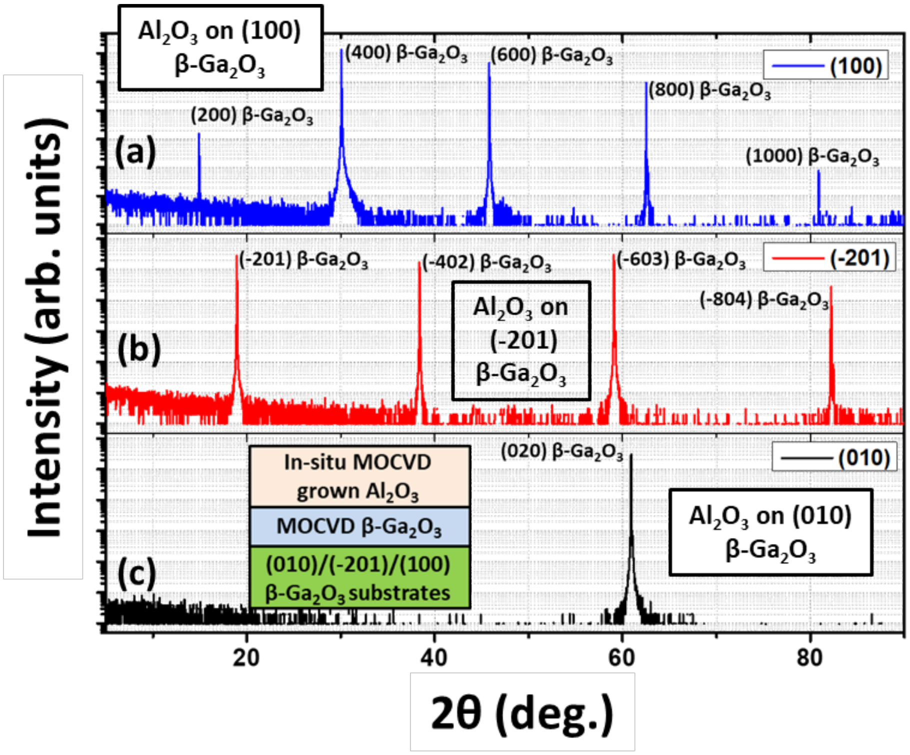
Al2O3 on (100) β-Ga2O3
(a)
(200) β-Ga2O3
(400) β-Ga2O3
(600) β-Ga2O3
(800) β-Ga2O3
(1000) β-Ga2O3
(100)
(b)
(-201) β-Ga2O3
(-402) β-Ga2O3
(-603) β-Ga2O3
(-804) β-Ga2O3
Al2O3 on (-201) β-Ga2O3
(-201)
(c)
In-situ MOCVD grown Al2O3
MOCVD β-Ga2O3
(010)/(-201)/(100) β-Ga2O3 substrates
(020) β-Ga2O3
(010)
Al2O3 on (010) β-Ga2O3
Intensity (arb. units)
20
40
60
80
2θ (deg.)

Figure 2.

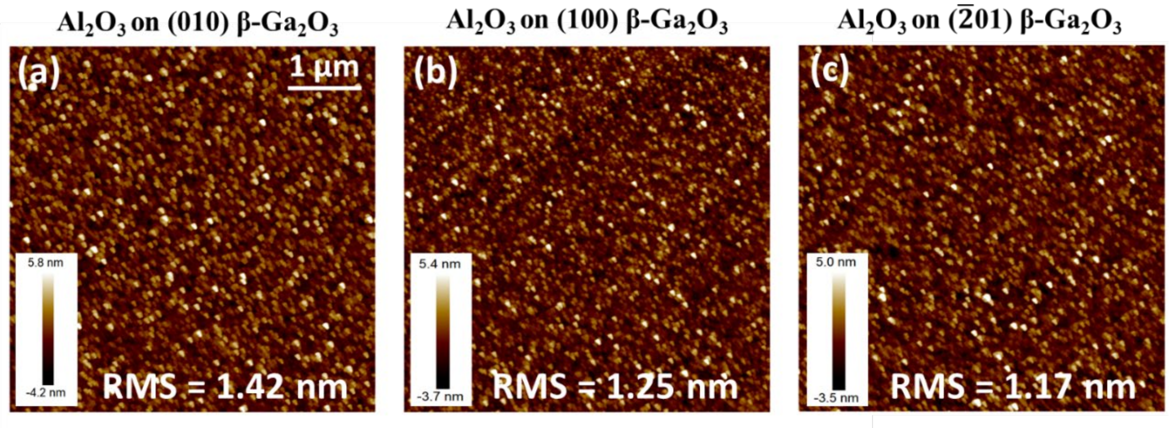

Al2O3 on (010) β-Ga2O3
Al2O3 on (100) β-Ga2O3
Al2O3 on (2̄01) β-Ga2O3
(a)
1 µm
5.8 nm
-4.2 nm
RMS = 1.42 nm
(b)
5.4 nm
-3.7 nm
RMS = 1.25 nm
(c)
5.0 nm
-3.5 nm
RMS = 1.17 nm

Figure 3.

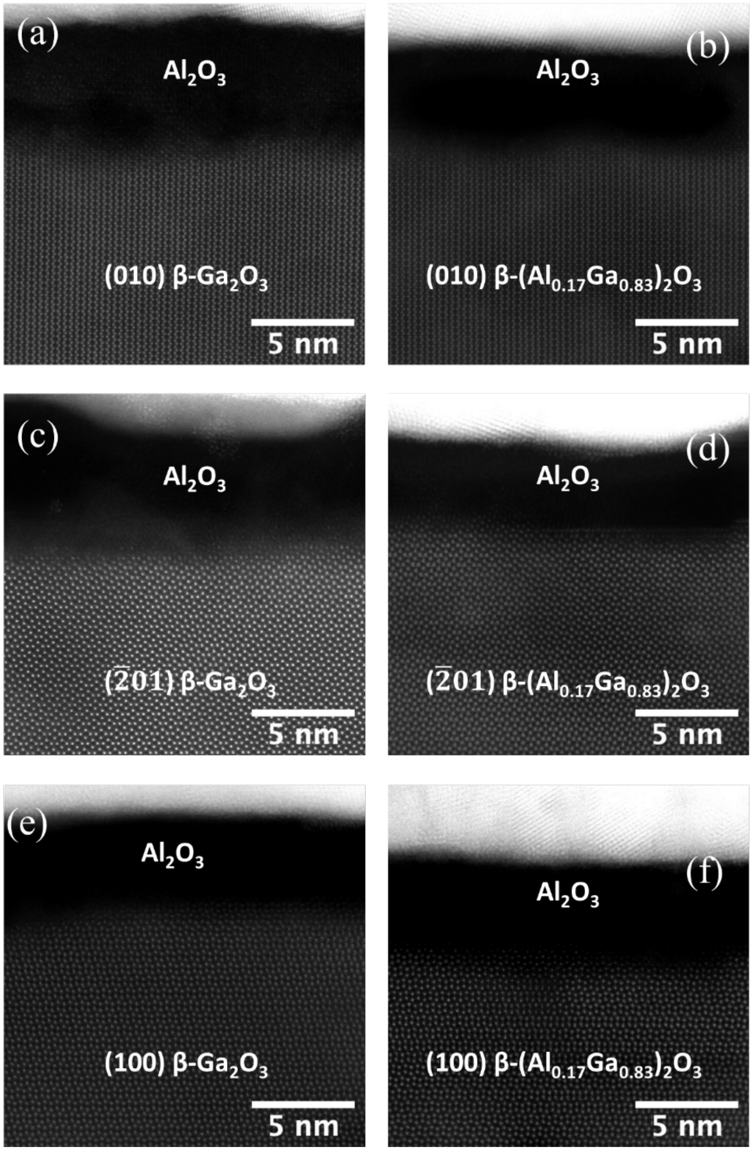
(a)
Al_2O_3
(010) β-Ga_2O_3
5 nm
(b)
Al_2O_3
(010) β-$(Al_{0.17}Ga_{0.83})_2O_3$
5 nm
(c)
Al_2O_3
$(\bar{2}01)$ β-Ga_2O_3
5 nm
(d)
Al_2O_3
$(\bar{2}01)$ β-$(Al_{0.17}Ga_{0.83})_2O_3$
5 nm
(e)
Al_2O_3
(100) β-Ga_2O_3
5 nm
(f)
Al_2O_3
(100) β-$(Al_{0.17}Ga_{0.83})_2O_3$
5 nm

Figure 4.

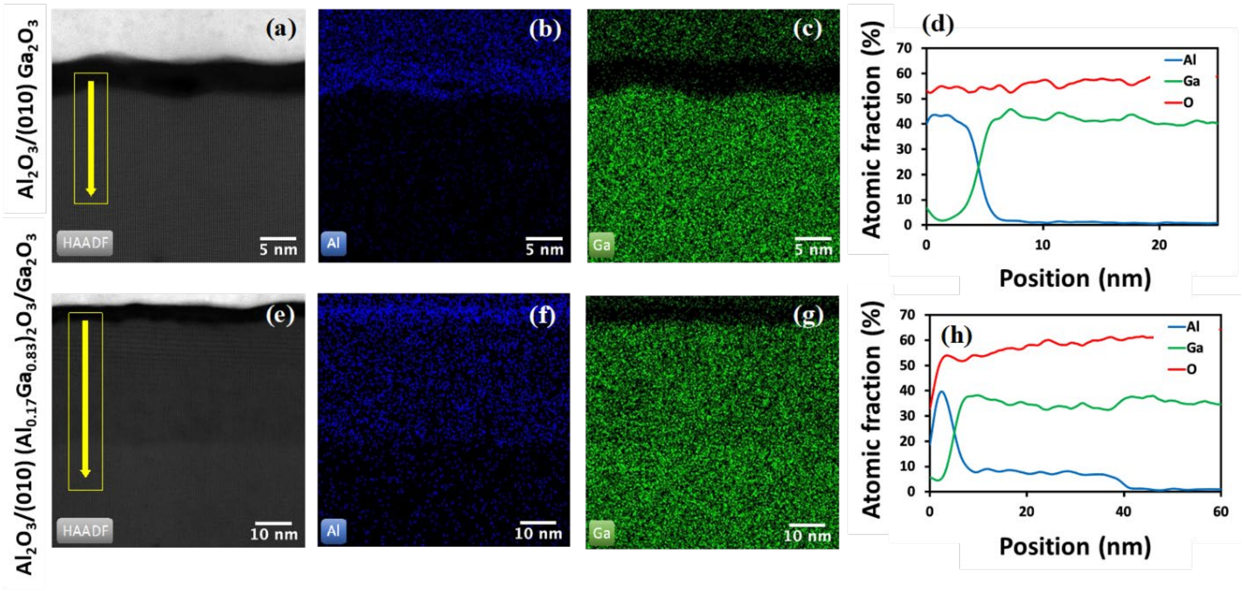

Al_2O_3/(010) Ga_2O_3
(a)
HAADF
5 nm
(b)
Al
5 nm
(c)
Ga
5 nm
(d)
Atomic fraction (%)
70
60
50
40
30
20
10
0
Al
Ga
O
0
10
20
Position (nm)
Al_2O_3/(010) $(Al_{0.17}Ga_{0.83})_2O_3$/$Ga_2O_3$
(e)
HAADF
10 nm
(f)
Al
10 nm
(g)
Ga
10 nm
(h)
Atomic fraction (%)
70
60
50
40
30
20
10
0
Al
Ga
O
0
20
40
60
Position (nm)

Figure 5.

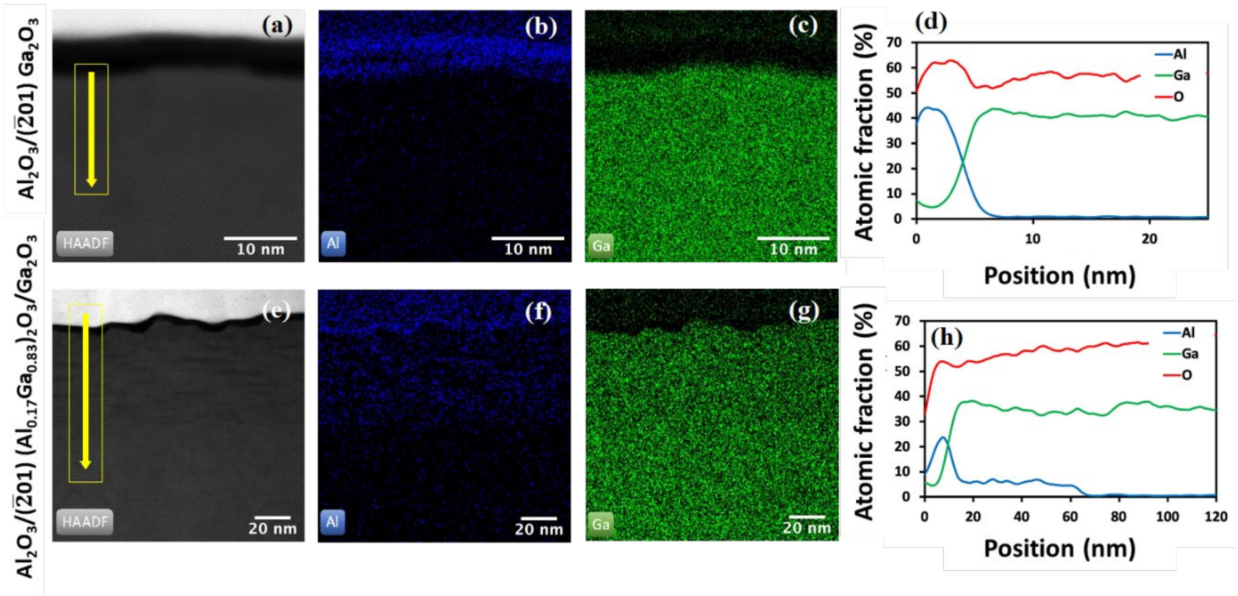
$Al_2O_3/(\bar{2}01)\ Ga_2O_3$
$Al_2O_3/(\bar{2}01)\ (Al_{0.17}Ga_{0.83})_2O_3/Ga_2O_3$
(a)
(b)
(c)
(d)
(e)
(f)
(g)
(h)
HAADF
Al
Ga
10 nm
20 nm
Atomic fraction (%)
Position (nm)
Al
Ga
O
0
10
20
30
40
50
60
70
80
100
120

Figure 6.

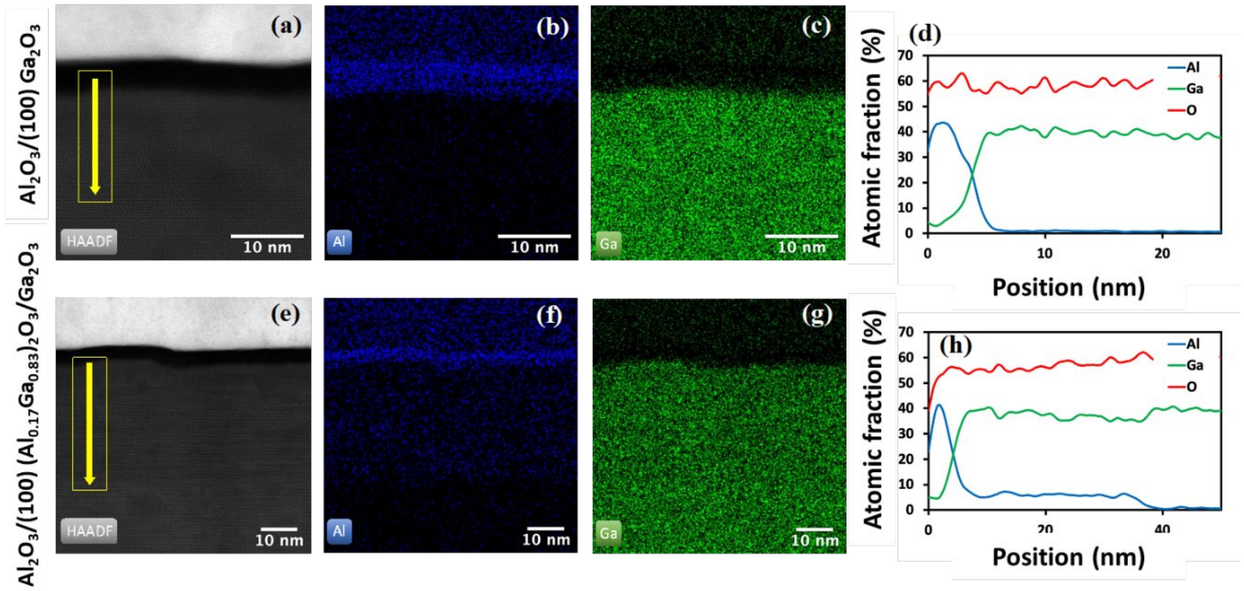
Al2O3/(100) Ga2O3
Al2O3/(100) (Al0.17Ga0.83)2O3/Ga2O3
(a)
(b)
(c)
(d)
(e)
(f)
(g)
(h)
HAADF
Al
Ga
10 nm
Atomic fraction (%)
Position (nm)
Al
Ga
O
0
10
20
30
40
50
60
70

Figure 7.

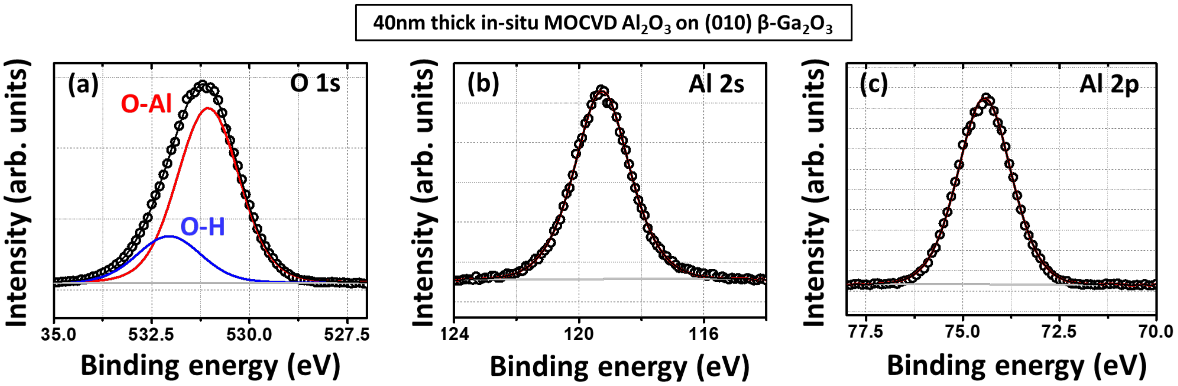
40nm thick in-situ MOCVD Al_2O_3 on (010) β-Ga_2O_3
(a)
O 1s
O-Al
O-H
Intensity (arb. units)
35.0
532.5
530.0
527.5
Binding energy (eV)
(b)
Al 2s
Intensity (arb. units)
124
120
116
Binding energy (eV)
(c)
Al 2p
Intensity (arb. units)
77.5
75.0
72.5
70.0
Binding energy (eV)

Figure 8.

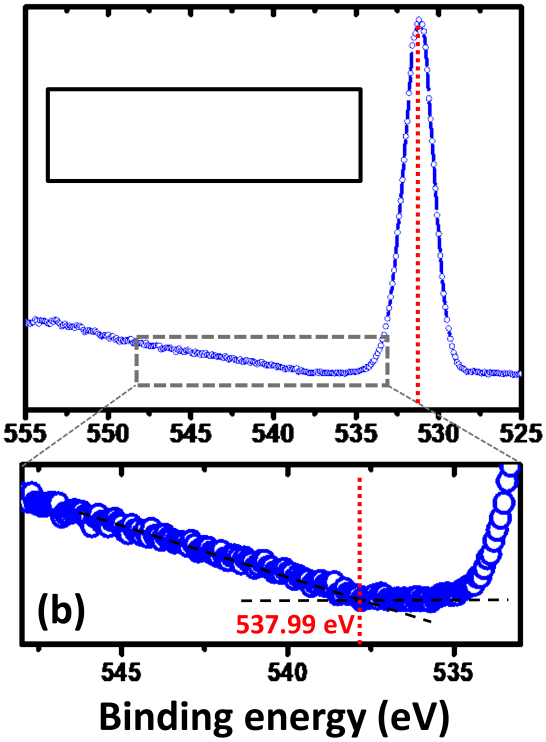
555
550
545
540
535
530
525
(b)
537.99 eV
545
540
535
Binding energy (eV)

Figure 9.

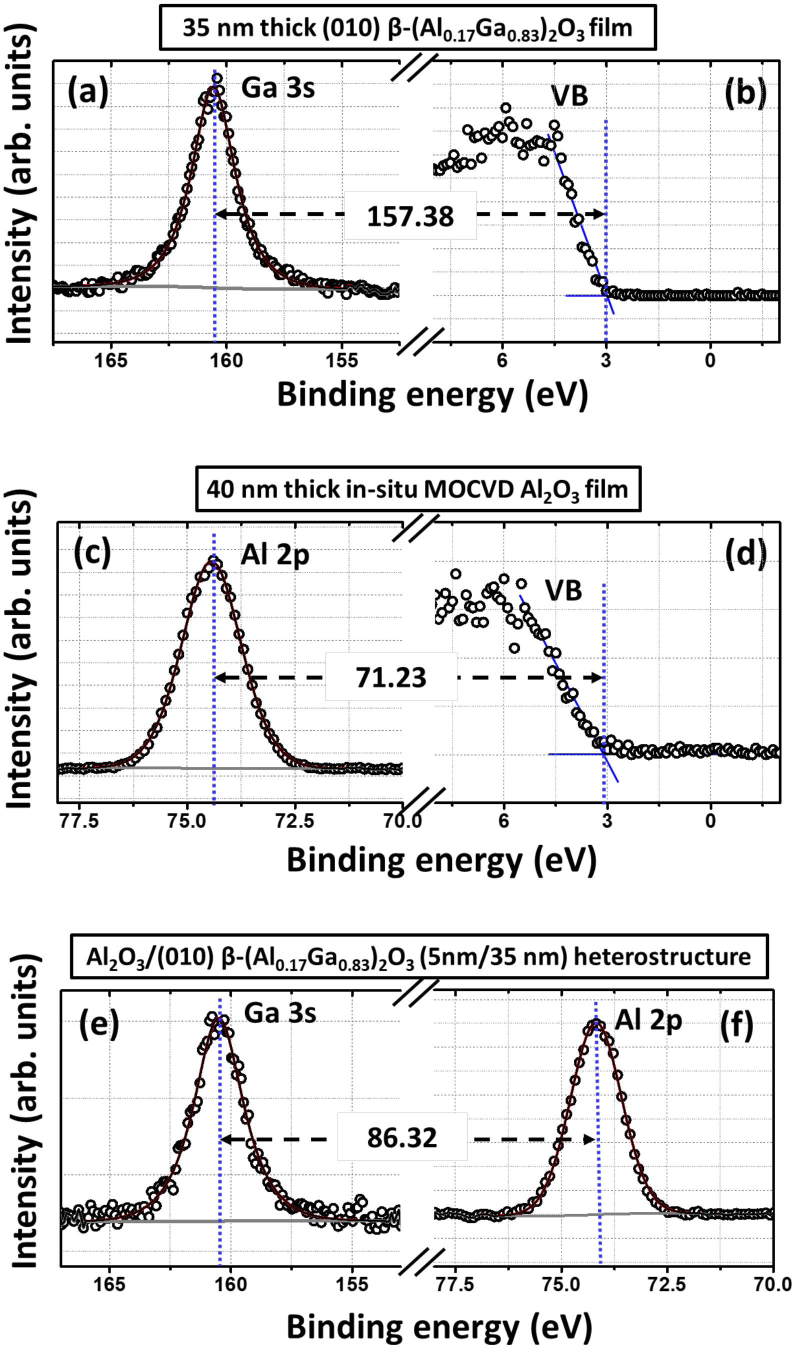
35 nm thick (010) β-(Al0.17Ga0.83)2O3 film
(a)
Ga 3s
VB
(b)
157.38
Intensity (arb. units)
165
160
155
6
3
0
Binding energy (eV)
40 nm thick in-situ MOCVD Al2O3 film
(c)
Al 2p
(d)
VB
71.23
Intensity (arb. units)
77.5
75.0
72.5
70.0
6
3
0
Binding energy (eV)
Al2O3/(010) β-(Al0.17Ga0.83)2O3 (5nm/35 nm) heterostructure
(e)
Ga 3s
Al 2p
(f)
86.32
Intensity (arb. units)
165
160
155
77.5
75.0
72.5
70.0
Binding energy (eV)

Figure 10.

(a) In-situ MOCVD Al_2O_3/(010) β-$(Al_xGa_{1-x})_2O_3$

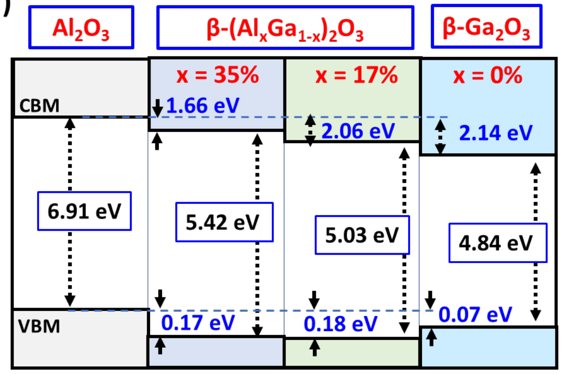

Type II band alignment

(b) In-situ MOCVD Al_2O_3/(100) β-$(Al_xGa_{1-x})_2O_3$

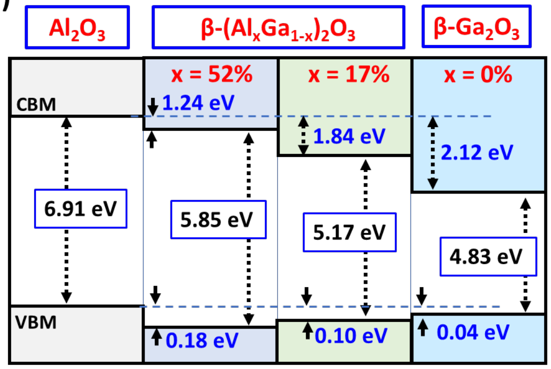

Type II band alignment

(c) In-situ MOCVD Al_2O_3/($\bar{2}01$) β-$(Al_xGa_{1-x})_2O_3$

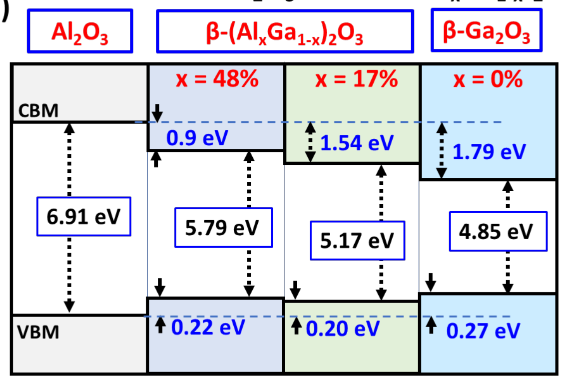

Type I band alignment

Figure 11.

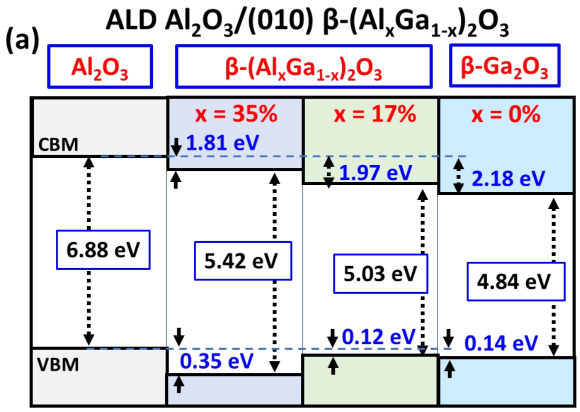

Type II band alignment

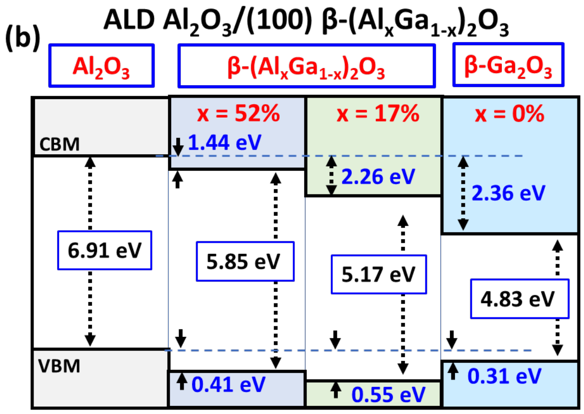

Type II band alignment

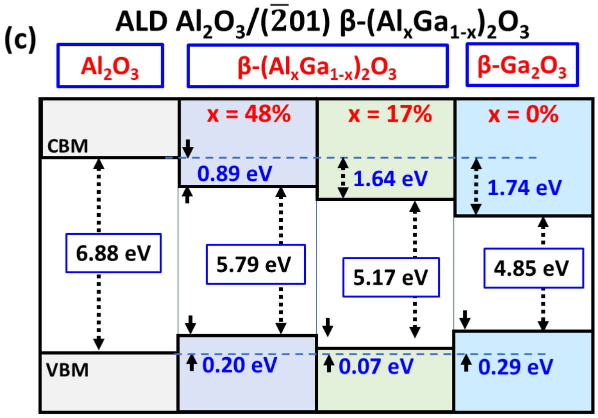

Type I band alignment

Figure 12.

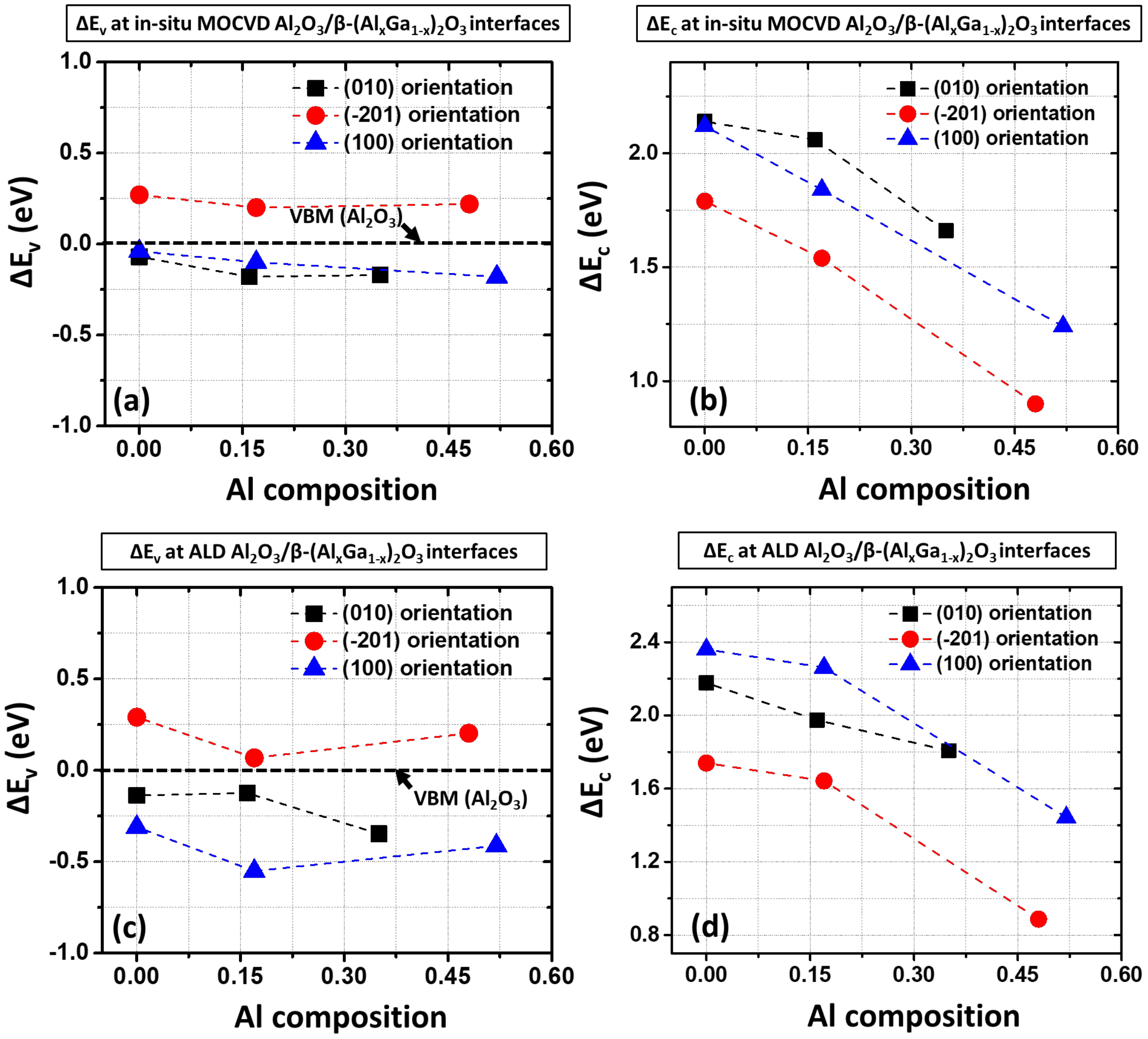

ΔE_v at in-situ MOCVD $Al_2O_3/\beta\text{-}(Al_xGa_{1-x})_2O_3$ interfaces

ΔE_c at in-situ MOCVD $Al_2O_3/\beta\text{-}(Al_xGa_{1-x})_2O_3$ interfaces

ΔE_v at ALD $Al_2O_3/\beta\text{-}(Al_xGa_{1-x})_2O_3$ interfaces

ΔE_c at ALD $Al_2O_3/\beta\text{-}(Al_xGa_{1-x})_2O_3$ interfaces